Porous Metal−Organic Polyhedral Frameworks with Optimal Molecular Dynamics and Pore Geometry for Methane Storage

Yong Yan,[†,¶] Daniil I. Kolokolov,[‡,§,¶] Ivan da Silva,[∥,¶] Alexander G. Stepanov,[‡,§] Alexander J. Blake,[⊥] Anne Dailly,[#] Pascal Manuel,[∥] Chiu C. Tang,[△] Sihai Yang,*[,†] and Martin Schröder*[,†,▽]

†School of Chemistry, University of Manchester, Oxford Road, Manchester, M13 9PL, United Kingdom

‡Boreskov Institute of Catalysis, Siberian Branch of Russian Academy of Sciences, Prospekt Akademika Lavrentieva 5, Novosibirsk 630090, Russia

§Novosibirsk State University, Pirogova Street 2, Novosibirsk 630090, Russia

∥ISIS Facility, Science and Technology Facilities Council (STFC), Rutherford Appleton Laboratory, Didcot, OX11 0QX, United Kingdom

⊥School of Chemistry, University of Nottingham, University Park, Nottingham, NG7 2RD, United Kingdom

#Chemical and Environmental Sciences Laboratory, General Motors Corporation, Warren, Michigan 48090, United States

△Diamond Light Source, Harwell Science and Innovation Campus, Didcot, Oxfordshire, OX11 0DE, United Kingdom

▽Nikolaev Institute of Inorganic Chemistry, Siberian Branch of the Russian Academy of Sciences, 3 Acad. Lavrentiev Avenue, Novosibirsk 630090, Russia

S *Supporting Information*

ABSTRACT: Natural gas (methane, CH_4) is widely considered as a promising energy carrier for mobile applications. Maximizing the storage capacity is the primary goal for the design of future storage media. Here we report the CH_4 storage properties in a family of isostructural (3,24)-connected porous materials, MFM-112a, MFM-115a, and MFM-132a, with different linker backbone functionalization. Both MFM-112a and MFM-115a show excellent CH_4 uptakes of 236 and 256 cm³ (STP) cm⁻³ (v/v) at 80 bar and room temperature,

respectively. Significantly, MFM-115a displays an exceptionally high deliverable CH_4 capacity of 208 v/v between 5 and 80 bar at room temperature, making it among the best performing metal−organic frameworks for CH_4 storage. We also synthesized the partially deuterated versions of the above materials and applied solid-state ²H NMR spectroscopy to show that these three frameworks contain molecular rotors that exhibit motion in fast, medium, and slow regimes, respectively. *In situ* neutron powder diffraction studies on the binding sites for CD_4 within MFM-132a and MFM-115a reveal that the primary binding site is located within the small pocket enclosed by the $[(Cu_2)_3(isophthalate)_3]$ window and three anthracene/phenyl panels. The open Cu(II) sites are the secondary/tertiary adsorption sites in these structures. Thus, we obtained direct experimental evidence showing that a tight cavity can generate a stronger binding affinity to gas molecules than open metal sites. Solid-state ²H NMR spectroscopy and neutron diffraction studies reveal that it is the combination of optimal molecular dynamics, pore geometry and size, and favorable binding sites that leads to the exceptional and different methane uptakes in these materials.
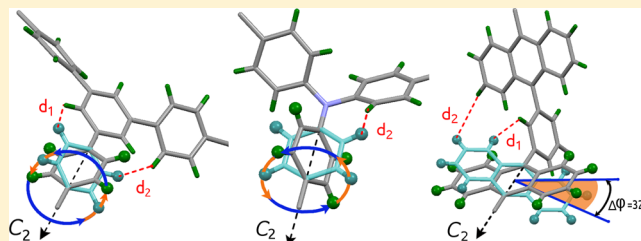
INTRODUCTION

Natural gas (comprised primarily of 95% methane, CH_4) has become an important fuel for mobile applications owing to its potentially reduced carbon emission at the point of use in comparison to gasoline-based hydrocarbon fuels.[1,2] Another key advantage of utilizing CH_4 as fuel lies in its abundant reserves and the widespread and mature infrastructure for its cost-viable recovery.[3] However, the extensive implementation of CH_4 as transportation fuel is restricted because of the underdevelopment of safe, efficient, and high-capacity storage systems. Therefore, challenges exist in the development of practical CH_4 storage materials that can outperform the state-of-the-art technologies mainly based upon liquefaction in

cryogenic tanks or compression in heavy-walled pressure vessels.[4]

Porous metal−organic framework (MOF) materials have attracted increasing research interest because of their potential applications in gas storage,[5−8] separation,[9,10] carbon capture,[11] small-molecule sensing,[12] and heterogeneous catalysis,[13] among others.[14,15] Constructed by bridging metal ions/clusters with organic ligands, crystalline MOFs have the unique advantage of extensive structural diversity and tunability.[16,17] The crystalline nature of MOFs allows advanced crystallographic analysis of
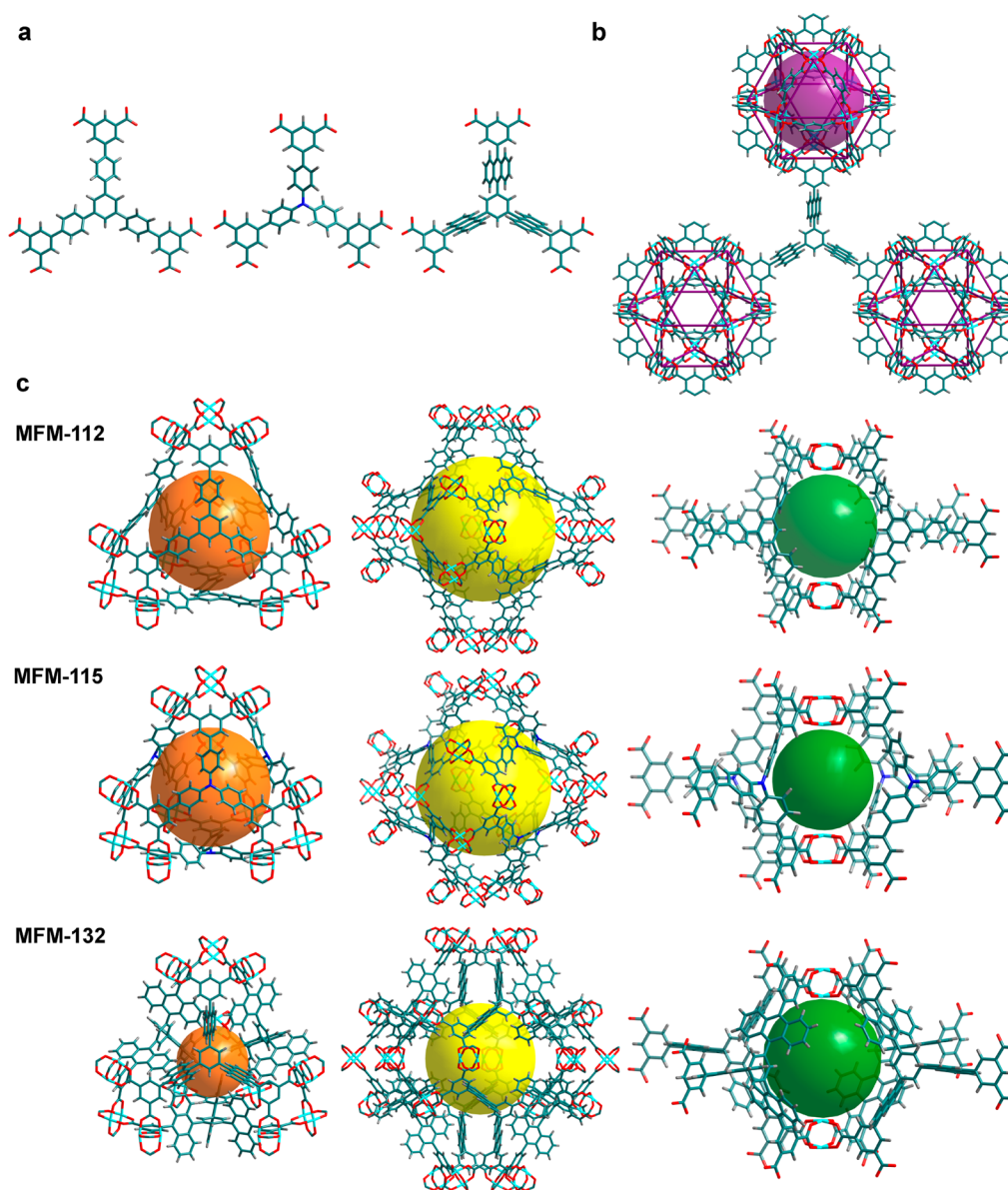
Figure 1. View of the chemical structures of the ligands and crystal structures of the isostructural MFMs series. (a) The three hexacarboxylate ligands for the construction of MFM-112, MFM-115, and MFM-132, respectively. (b) In the (3,24)-connected network, the linker with C_3-symmetry is connected to three cuboctahedra (cage A). The MFM-132 case is shown as an example. (c) The different cage structures (cage B, C, and D) in the above three frameworks. The colors for the spheres that fit into the void of different types of cages are magenta for cage A, orange for cage B, yellow for cage C, and green for cage D.

the structural change upon external stimuli and/or the host−guest interactions.[18] These structural insights at a molecular level can effectively direct the design of future MOFs showing optimized capability of binding guest molecules for enhanced storage/separation performance. In the context of CH_4 storage, the primary target for materials design is to maximize the adsorption capacity and more importantly the deliverable capacity with the aim of approaching the DOE target for on-board CH_4 storage.[19]

The synthesis of MOFs based on Cu(II) with isophthalate ligands[20] has been proved to be an effective strategy to achieve high CH_4 storage capacity.[21] A family of robust (3,24)-connected networks with ultrahigh porosity incorporating hexacarboxylate ligands and $[Cu_2(O_2CR)_4]$ paddlewheels has been reported to show exceptional gas adsorption properties.[21−25] Open metal sites can provide strong affinity for CH_4,

as evidenced by previous structural studies on several MOFs such as $Cu_3(BTC)_2$ (BTC^{3-} = benzene-1,3,5-tricarboxylate)[26−28] and Mg-MOF-74.[29] However, open metal sites often saturate rapidly upon guest uptake and thus have a limited role in defining the maximum gas capacity. This is particularly the case at high pressure, where adsorbate−adsorbate interactions dominate the uptake process. However, the effects of optimizing the configuration and molecular dynamics of the ligand core have been largely overlooked for the enhancement of overall CH_4 adsorption capacity.

We report here the CH_4 adsorption properties in a series of (3,24)-connected MOFs, MFM-112,[22] MFM-115,[24b] and MFM-132 (MFM = Manchester Framework Material replacing the NOTT specification), incorporating a central phenyl ring, a nitrogen center at the core of the hexacarboxylate, and anthracene functionalization, respectively. Thus, variation of

the central part of the hexacarboxylate ligands where three isophthalate units are covalently connected in a coplanar fashion results in structures with different functionalities and pore geometries. Significantly, desolvated MFM-115a shows an exceptionally high deliverable CH_4 capacity of 208 cm^3 (STP) cm^{-3} (v/v) between 5 and 80 bar at room temperature, making it among the best performing porous materials for CH_4 storage. In most porous MOF structures, the organic linker contains mobile aromatic fragments that can rotate around a certain axis within the void. This rotation creates dynamic disorder in the framework, which effectively changes the inner geometry of the pore, as well as the positions of possible adsorption sites associated with the fragment. We report also the molecular dynamics of the rotationally dynamic aromatic rings in the partially deuterated isostructural series (desolvated MFM-112a-d_{12}, MFM-115a-d_{12}, and MFM-132a-d_{24}) as revealed by solid-state ^{2}H NMR spectroscopy. We confirm how these dynamics can be controlled in a simple manner by rational synthesis. In addition, neutron diffraction studies on CD_4-loaded MFM-132a and MFM-115a afford precise details of CD_4 binding in these two structures at a molecular level. In MFM-132a, a tight pocket of 6 Å diameter is formed by the anthracene rings close to the $[(Cu_2)_3(isophthalate)_3]$ window, and this shows an affinity for CD_4 that surprisingly is stronger than at the open Cu(II) sites. Interestingly, CD_4 in MFM-115a shows optimum packing efficiency within this porous structure.

■ RESULTS AND DISCUSSION

Structures and Porosity of MFM-112, MFM-115, and MFM-132. The three isostructural MOFs all have (3,24)-connected networks, where $[Cu_2(O_2CR)_4]$ paddlewheels are bridged by the isophthalate units from the hexacarboxylate ligands to form cuboctahedra, which are further connected by the central triangular ligand core (Figure 1). In the structure of MFM-132, a $[Cu_{24}(isophthalate)_{24}]$ cuboctahedron (cage **A**), constructed from 12 {Cu$_2$} paddlewheels and 24 isophthalates (from 24 independent BTAT^{6-} units) [H$_6$BTAT = 5,5′,5″-(benzene-1,3,5-triyltris(anthracene-10,9-diyl))triisophthalic acid], is heavily shielded by 24 anthracene units from different ligands. Upon removal of coordinated water molecules from the axial sites of the metal ions, the interior accessible void in cage **A** is ~1.3 nm in diameter. This cage possesses a highly hydrophobic outer shell (anthracene panels) and an internal hydrophilic cavity [12 open Cu(II) sites in its activated phase] and is anticipated to show highly confined host−guest binding properties. Cage **B**, a truncated tetrahedron comprising four ligands and four $[Cu_6(isophthalate)_3]$ triangular windows, with 12 anthracene units protruding into the central void, shows a diminished cage size of 6.5 Å (defined as the diameter of the largest sphere that can be fitted into the cavity taking into account the van der Waals radii of surface atoms). This is much smaller than that of the phenylene-functionalized MFM-112 (cage **B** ≈ 14 Å in diameter). The truncated octahedral cage **C** is constructed from eight BTAT^{6-} units and six $[Cu_8(isophthalate)_4]$ square windows and possesses an accessible void 13 Å in diameter despite having 24 anthracene rings protruding into the center of the cavity. The void between the two closest cuboctahera or the fused cages **B** and **C** generates the fourth cage, cage **D**, which is composed of eight anthracene panels from four ligands and two $[Cu_2(O_2CR)_4]$ paddlewheels with an enclosed spherical cavity of 10 Å in diameter and small apertures of 5 Å × 5 Å. Overall, the anthracene functionalization in MFM-132 yields a rich
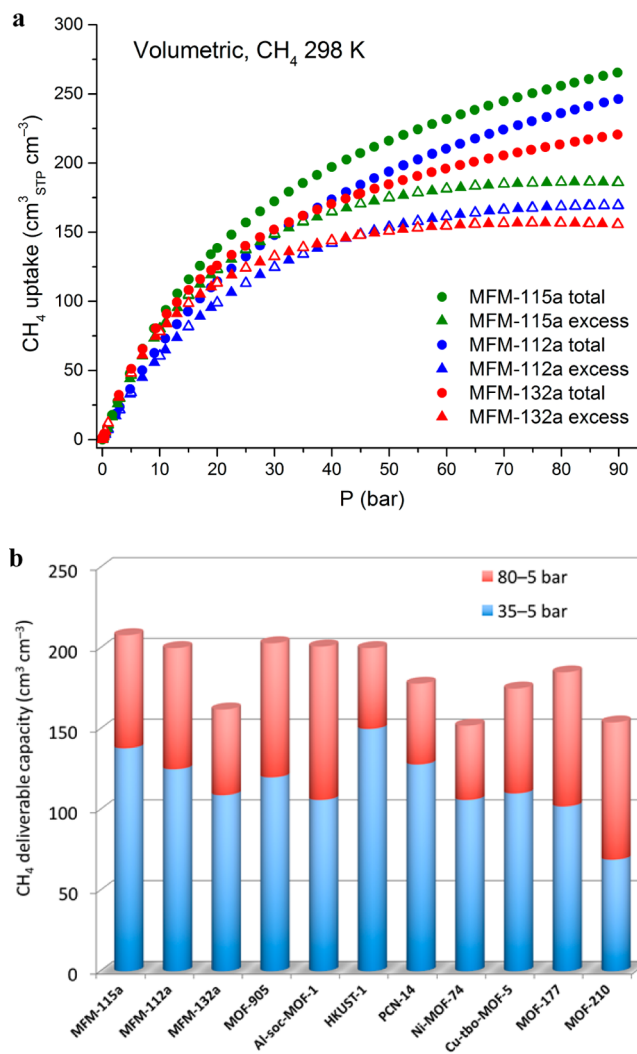

Figure 2. Comparison of high-pressure CH_4 adsorption data for the best-performing MOFs. (a) High-pressure volumetric CH_4 adsorption isotherms for MFM-115a, MFM-112a, and MFM-132a in the pressure range 0−90 bar at 298 K. (b) Comparison of the deliverable CH_4 capacity for a range of MOFs at 298 K.

combination of metal−organic coordination cages of different geometry, size, and pore surface chemistry, thus representing a unique platform to study the host−guest binding in porous materials.

The three MOFs show similar thermal stability with framework decomposition at 350 °C, as confirmed by thermogravimetric analyses (Figure S9).[22,24b] The desolvated samples of MFM-112a, MFM-115a, and MFM-132a can be readily prepared by removing the free and coordinated solvent molecules from the pore at 100 °C under dynamic vacuum. The desolvated materials show retention of the framework structure as confirmed by PXRD analysis. The solvent-accessible void calculated using PLATON/VOID[30] for MFM-132a is 63%, lower than that of MFM-112a (75%) and MFM-115a (72%) owing to the anthracene functionalization. Unsurprisingly, MFM-132a shows a lower Brunauer−Emmett−Teller (BET) surface area (S_{BET} = 2466 m^2 g^{-1}) and total pore volume (V_p = 1.06 cm^3 g^{-1}) than that of MFM-112a (S_{BET} = 3800 m^2 g^{-1}; V_p = 1.62 cm^3 g^{-1}) and MFM-115a (S_{BET} = 3394 m^2 g^{-1}; V_p = 1.38 cm^3 g^{-1}). The pore size distribution calculated using the NLDFT method indicates a homogeneous

Table 1. Comparison of CH$_4$ Adsorption Data for a Variety of MOFs at 298 K

material	BET surface area (m^2/g)	pore volume (cm^3/g)[b]	crystal density (g/cm^3)	total uptake at 35 bar	deliverable CH$_4$ capacity (5 to 35 bar)	total CH$_4$ uptake at 65 bar	deliverable CH$_4$ capacity (5 to 65 bar)	total uptake at 80 bar	deliverable CH$_4$ capacity (5 to 80 bar)
				v/v	v/v	v/v	v/v	v/v	v/v
MFM-115a	3394	1.38	0.611	186	138	238	191	256	208
MFM-112a	3800	1.62	0.503	162	125	218	181	236	200
MFM-132a	2466	1.06	0.65	162	109	201	150	213	162
Co(bdp)[38]	2911[a]	1.02	0.774	161	155	203	197		
MOF-905[40]	3490	1.34	0.537[d]	145	120	206	181	228	203
Al-soc-MOF-1[41]	5585	2.3	0.34	127	106	197	176	221	201
MOF-519[35,40]	2400	0.938	0.953	200[c]	151[c]	260[c]	209[c]	279[c]	230[c]
UTSA-76a[39]	2820	1.09	0.699	211	151	257	196		
HKUST-1[7,31]	1850	0.78	0.883	227	150	267	190	272	200
PCN-14[7,31,36]	2000	0.85	0.829	195	128	230	157	250	178
NU-125 (NOTT-122a)[24a,31,37]	3286	1.41	0.589	182	135	232	183		
Ni-MOF-74[7,29,31]	1350	0.51	1.206	228	106	251	129	267	152
Cu-tbo-MOF-5[42]	3971	1.12	0.595	151	110	199	158	216	175
MOF-177[43]	4500	1.89	0.427	122	102			205	185
MOF-210[43]	6240	3.6	0.25	82	69	141	128	166	154

[a]Langmuir surface area. [b]Pore volume was measured by N$_2$ adsorption isotherms at 77 K. [c]These values are likely overestimated due to difficulty in controlling composition of MOF-519.[40] [d]Crystal density determined from pycnometer density data.

distribution of pore size of ~12 Å in MFM-132a. MFM-112a and MFM-115a show a hierarchical pore system comprising different-sized pores, with the largest pore size being 17 and 20 Å, respectively. Because of the presence of bulky aromatic groups, MFM-132a has a calculated crystal density of 0.650 g cm^{-3}, higher than that of MFM-112a (0.503 g cm^{-3}) and MFM-115a (0.611 g cm^{-3}).[20] Throughout this and other reports, it is common practice for the volumetric gas uptake to be derived from the bulk material density based upon the single-crystal structure, but it should be noted that when the efficiency of packing and the polycrystalline nature of the bulk material are considered, the uptakes will be reduced accordingly; this will be subject to the different compressibility and mechanical stability of different materials.

CH$_4$ Storage. Adsorption measurements were performed using a gravimetric adsorption analyzer for the desolvated materials at 298 K over the pressure range of 0–90 bar (Figures 2, S11). The excess CH$_4$ uptakes in these materials increase with increasing pressure until reaching the maximum in a high-pressure region (80–90 bar). The total CH$_4$ uptake was calculated from the excess uptake by including the amount of compressed CH$_4$ in the pore using the pore volume as determined from N$_2$ isotherms. Although MFM-112a shows higher gravimetric CH$_4$ uptakes than MFM-115a in the high-pressure range (30–90 bar), the volumetric uptakes show the opposite trend due to the higher crystal density of MFM-115a. At 35 bar, MFM-112a and MFM-115a show high total gravimetric CH$_4$ uptakes of 322 and 304 cm^3 (STP) g^{-1}, respectively, comparable to those measured for the best-behaving MOFs under the same conditions.[31–34] In addition, MFM-115a shows a high volumetric total CH$_4$ capacity of 186 v/v when compared to other high-performing CH$_4$ uptake materials such as MOF-519,[35] PCN-14,[36] and NU-125[24a,31,37] at 35 bar and 298 K. In comparison, MFM-112a has a lower total volumetric CH$_4$ uptake of 162 v/v at 35 bar. Although MFM-132a shows lower total gravimetric CH$_4$ uptake of 249 cm^3 (STP) g^{-1} than MFM-112a, it has the same volumetric

uptake of 162 v/v at 35 bar and 298 K owing to the higher crystal density of MFM-132a. At 80 bar, MFM-115a and MFM-112a both show remarkable increases in their total CH$_4$ adsorption capacities to 419 and 469 cm^3 g^{-1}, equivalent to volumetric uptakes of 256 and 236 v/v, respectively. MFM-132a has a lower surface area and pore volume, resulting in a lower uptake of 213 v/v compared to MFM-112a and MFM-115a at 80 bar and 298 K.

The deliverable capacity, defined as the amount of CH$_4$ released from the storage system between a high-pressure stage (generally 65–80 bar) and a low-pressure stage (typically 5 bar), is of direct relevance to the practical performance of a given storage medium. MFM-115a and MFM-112a show high deliverable CH$_4$ capacities of 191 v/v and 181 v/v between 65 and 5 bar at 298 K, respectively, comparable with the best performing CH$_4$ storage materials such as [Co(bdp)][38] (bdp^{2-} = 1,4-benzenedipyrazolate) (197 v/v) and UTSA-76a (196 v/v).[39] Significantly, MFM-115a exhibits an exceptionally high deliverable CH$_4$ capacity of 208 v/v between 80 and 5 bar at room temperature, rivaling those reported for the state-of-the-art materials (Figure 2b, Table 1) such as MOF-905 (203 v/v),[40] Al-soc-MOF-1 (201 v/v),[41] and HKUST-1 (200 v/v).[31] MFM-112a also exhibits an excellent performance in delivering 200 v/v of CH$_4$ between 80 and 5 bar at 298 K. In contrast, compared to both MFM-112a and MFM-115a, MFM-132a shows lower deliverable (to 5 bar) CH$_4$ capacities of 150 and 162 v/v at 65 and 80 bar, respectively. The isosteric heats of adsorption (Q_{st}) at low CH$_4$ loading are estimated to be 16.2, 16.3, and 15.7 kJ mol^{-1} for MFM-112a, MFM-115a, and MFM-132a, respectively. These values are comparable to other MOFs with open Cu(II) sites.[26,32]

Comparison of the CH$_4$ adsorption in these three materials reveals interesting findings. MFM-115a, with moderate porosity across this series of MOFs, displays the highest methane deliverable capacity, outperforming MFM-112a, which shows slightly higher surface area and pore volume. The only structural difference between MFM-112a and MFM-115a lies
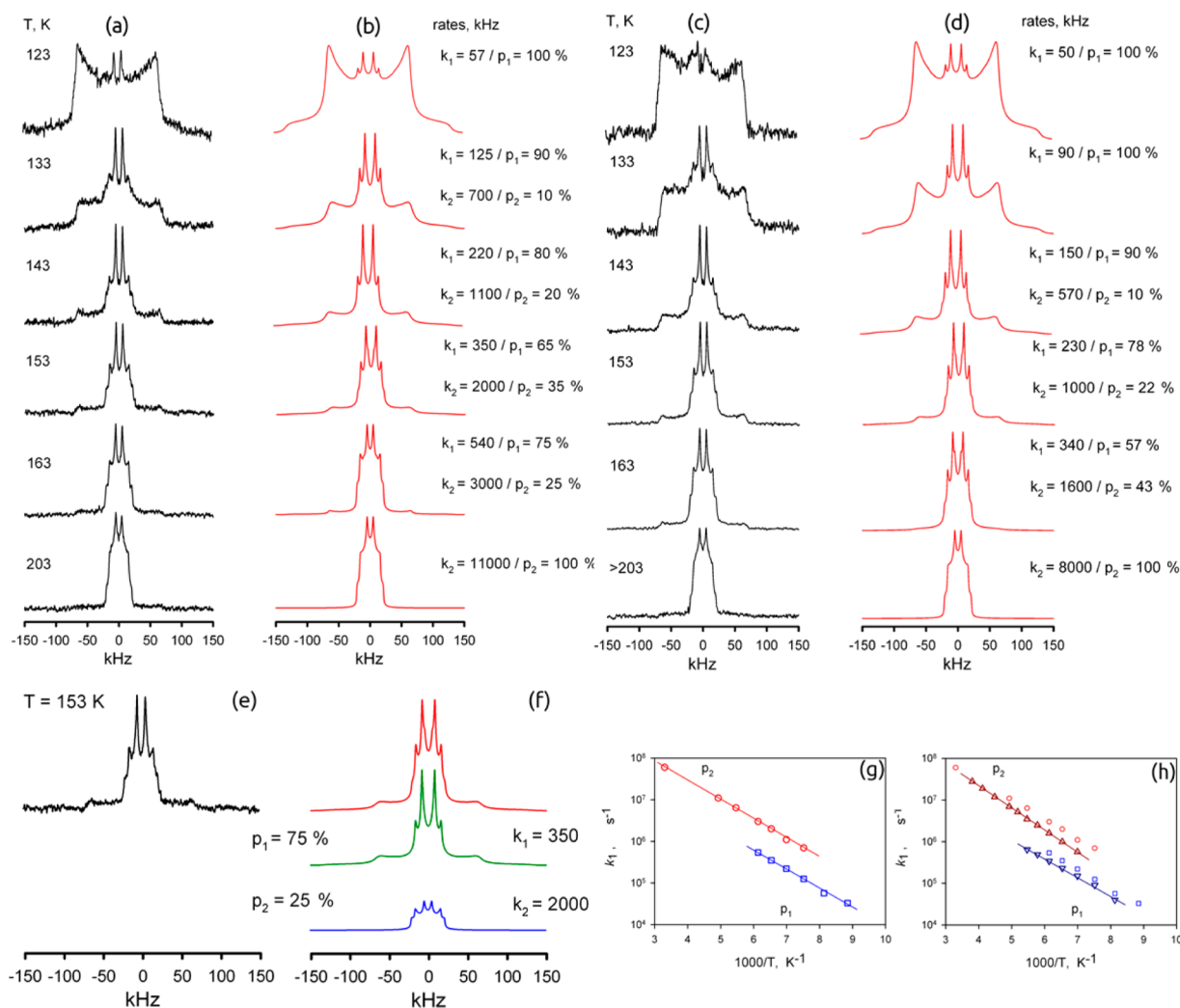
Figure 3. Temperature-dependent ^{2}H NMR line shapes for the deuterated phenylene fragments in guest-free MFM-112a-d_{12}: (a) experimental and (b) simulation; MFM-112a-d_{12} loaded with CH$_4$ (10 bar at 298 K): (c) experimental and (d) simulation. (e) ^{2}H NMR spectrum for the guest-free MFM-112a-d_{12} comprising (f) two dynamic phases at $T = 153$ K. (g) Arrhenius plots of the rotation rate constants k_1 ($\square$) and k_2 ($\bigcirc$) for the two corresponding phases of the guest-free MFM-112a-d_{12} and (h) k_1 (∇) and k_2 ($\triangle$) for MFM-112a-d_{12} loaded with CH$_4$ at 10 bar and 298 K.

in the central triangular organic moiety of the hexagonal linker face (Figure 1). We therefore argued that the pore environment created by the rotating phenylene rings in the linker can affect and perhaps control the gas adsorption properties of the host materials.

^{2}H NMR Spectroscopic Studies. Solid-state ^{2}H NMR spectroscopy was used to investigate the molecular dynamics of the rotating aromatic rings in this series of MOFs. This is a very powerful experimental technique well suited to monitor the molecular reorientations over a wide range of characteristic rates ($10^3 - 10^7$ s^{-1}) and geometries (angular displacement >5°) in the solid state.[44,45] The three MOFs were partially deuterated by selectively introducing D atoms on the aromatic rings in the ligands (see Supporting Information Section S4). The solid-state ^{2}H NMR spectra for MFM-112a-d_{12}, MFM-115a-d_{12}, and MFM-132a-d_{24} were collected over a range of temperatures (100−525 K, up to the temperature limit of the NMR magnet probe) to follow their structural dynamics (Figures 3, 5, and 6). The molecular motion was analyzed by the evolution of the ^{2}H NMR line shape arising from the perdeuterated fragments in the frameworks in a given temperature range. The temperature evolution of the ^{2}H
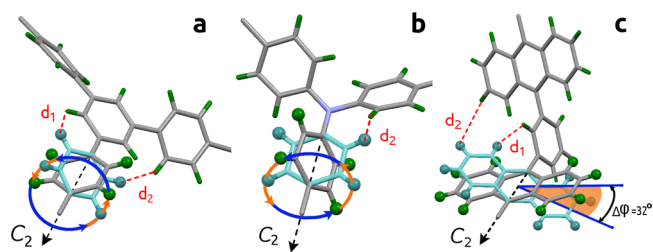

Figure 4. View of the rotational models probed by solid-state ^{2}H NMR spectroscopy for the partially deuterated MFM series in this study: (a) MFM-112a-d_{12}, (b) MFM-115a-d_{12}, and (c) MFM-132a-d_{12}.

NMR line shape typically involves three stages: (i) static, when $k < 10^3$ s^{-1} (the rotational rate constant) with the line shape dependent solely on the electronic configuration of the C−D bond; (ii) intermediate exchange with $10^3 < k < 10^7$ s^{-1} with the line shape reflecting both the rate and the geometry of the motion; and (iii) fast limit when $k > 10^7$ s^{-1} with an averaged line shape reflecting the final geometry but not the rate of the molecular orientation (Figure S20). We probed as wide a
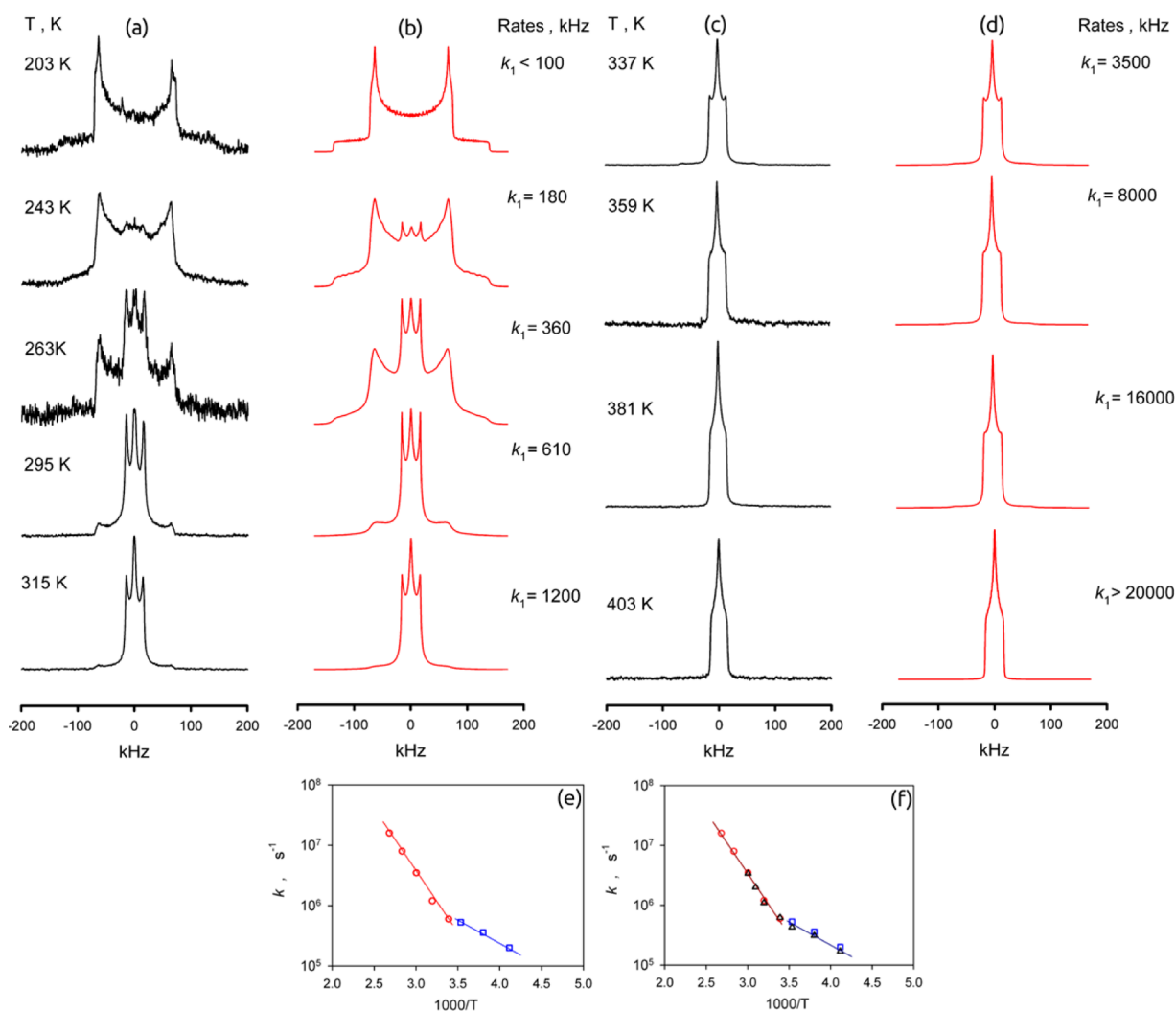
Figure 5. Temperature-dependent ^2H NMR line shapes for the deuterated phenylene fragments in guest-free MFM-115a-d_{12}: (a, c) experimental and (b, d) simulation. (e) Arrhenius plots of the rotation rate constant k_1 (○ and □) for the guest-free MFM-115a-d_{12} and (f) k_1 (△) for the MFM-115a-d_{12} framework loaded with CH_4 at 10 bar and 298 K.

temperature range as possible to study the most informative, intermediate exchange regime for each material.

MFM-112a-d_{12}. As shown in Figure 3, the numerical line shape analysis indicates that the rotation of the phenylene fragment in MFM-112a-d_{12} is realized by a four-site jump exchange between four positions given by the following axial angles: $\varphi_1 = 40°$, $\varphi_2 = 140°$, $\varphi_3 = 220°$, $\varphi_4 = 320°$ (Figure 4 and Figure S21). Interestingly the ^2H NMR spectroscopic data reveal two dynamically different states for rotation of the linker in MFM-112a-d_{12}. In each state the geometry of the rotation is the same, but the rate at each temperature is different. These two dynamic phases (states) of MFM-112a-d_{12} coexist between 133 and 163 K. Below 133 K the material is the phase $\mathbf{p_1}$ (rate k_1), while above 163 K it fully switches to phase $\mathbf{p_2}$ (rate k_2). In both states the corresponding rate constants k_1 and k_2 obey the simple Arrhenius law (Figure 3g) and are characterized by the same activation barrier ($E = 8.6$ kJ mol^{-1}). The only difference is in the pre-exponential (collision) factor, which differs by a factor of six: $k_{1,0} = 3 \times 10^8$ s^{-1}, $k_{2,0} = 18 \times 10^8$ s^{-1}. The nature of these two states requires additional investigation, and the change of the dynamic state for the mobile fragment in the linker in MFM-112-d_{12} is most likely associated with the change of the steric interactions between the rotating phenylene rings

and the central immobile phenyl ring at different temperatures.[46]

Line shape analysis for MFM-112a-d_{12} loaded with CH_4 (10 bar of equilibrium pressure above the MOF at 298 K in a sealed glass NMR cell) (Figure 3c,d) shows that the linker rotation mechanism remains unchanged, but the actual rates are affected as the CH_4 guest molecules partially block the linker rotation.[47] The corresponding rates and temperature dependences are shown in Figure 3h. It follows that for the low-temperature phase $\mathbf{p_1}$ the effect of CH_4 presence is reflected in the collision factor, which is smaller by a factor of ~0.62 relative to the guest-free material. The second phase $\mathbf{p_2}$ is also characterized by a smaller rotation rate compared to the guest-free material, but the barrier is slightly increased up to $E \approx 10$ kJ mol^{-1} ($k_{2,0} = 29 \times 10^8$ s^{-1}). However, it should be noted that this small increase in activation energy is most likely related to the partial desorption of CH_4 from the pores above 200 K.

MFM-115a-d_{12}. As shown in Figure 5 the line shape develops from a static pattern to a dynamically averaged one between 203 and 315 K. However, in the static case, the pattern is characterized by a nuclear quadrupolar coupling constant $Q_0 = 184$ kHz and an asymmetry parameter $\eta_0 = 0.06$, which is unusual and shows how strongly the electronic state of the
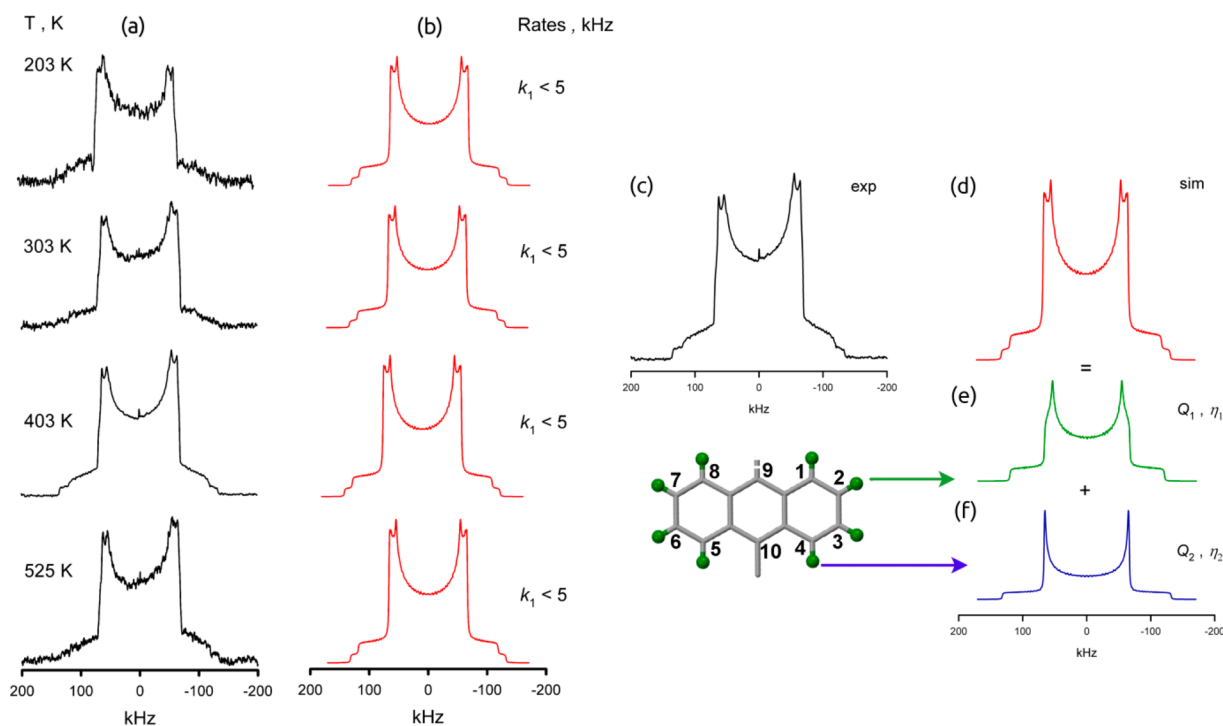
Figure 6. Variable-temperature ^{2}H NMR line shapes for MFM-132-d_{24}: (a) experimental and (b) simulation. The ^{2}H NMR spectrum of MFM-132-d_{24}, (c) experimental and (d) simulation, is composed of two signals (e and f), which correspond to geometrically different C−D groups on the anthracene fragment. The green spheres represent deuterium atoms.

mobile phenylene groups is distorted by the nitrogen core of the ligand. The averaged pattern is given by a narrowed line shape, as expected for axial rotation of the phenylene groups around the C_2 symmetry axis ($Q_1 \approx 20$ kHz $\approx Q_0/8$).[48] However, the narrowed patterns are characterized by an even larger asymmetry parameter $\eta \approx 1$, indicating that the geometry of the rotation is different from that in MFM-112a-d_{12}. As observed in the Arrhenius plot (Figure 5e), the temperature dependence of the exchange rate constant k is characterized by two regions: below 283 K the motion is characterized by a barrier $E = 14$ kJ mol^{-1} and a collision factor $k_0 = 2 \times 10^8$ s^{-1}; above 283 K the barrier increases to $E = 40$ kJ mol^{-1} and a collision factor $k_0 = 5 \times 10^{12}$ s^{-1}. The mechanism of rotation is given by a four-site jump rotation, but above 283 K the six-site jump rotation gives slightly better agreement with the experimental patterns (Figure S21). The positions for the four-site rotation are given by the following axial angles: $\varphi_1 = 42°$, $\varphi_2 = 138°$, $\varphi_3 = 222°$, $\varphi_4 = 318°$. Those for the positions for the six-site rotation are $\varphi_1 = 42°$, $\varphi_2 = 90°$, $\varphi_3 = 138°$, $\varphi_4 = 222°$, $\varphi_5 = 270°$, $\varphi_6 = 318°$.

Such drastic changes in both activation barrier and the pre-exponential factor indicate that there are two possible rotational stochastic mechanisms that compete, with the ^{2}H NMR line shape reflecting the faster motion. In MFM-115a-d_{12} the three rotating phenylene groups are bound to a single N-center, and hence their steric interaction is expected to be notably stronger than in MFM-112a-d_{12}. Thus, the individual rotation of each phenylene ring is expected to be characterized by a high activation energy and a normal pre-exponential factor of $\sim 10^{12}$ s^{-1}. However, since the three phenylene groups create a molecular "gear-like" mechanism, we might expect correlated rotation. In such a case the overall activation barrier might be expected to be much lower compared to individual rotations. However, the chance for such cooperative motion occurring

(i.e., the number of attempts) is much lower as well. Therefore, the low-energy mode is characterized by a much lower pre-exponential factor of $\sim 10^8$ s^{-1}. To our knowledge, this is the first example of direct observation of how the cooperative molecular rotations in MOFs are switched to an individual motif.

The CH$_4$-loaded sample of MFM-115a-d_{12} (10 bar of equilibrium pressure above the MOF at 298 K in a sealed glass NMR cell) showed identical line shape and temperature dependence compared to the guest-free material. The corresponding rate constants are shown in Figure 5f. Thus, the effect of CH$_4$ on the rotation of the phenylene rings in MFM-115a-d_{12}, even at elevated pressure, is negligible, probably reflecting the higher temperatures required for rotational mobility in MFM-115a-d_{12} compared with MFM-112a-d_{12}.

MFM-132-d_{24}. The ^{2}H NMR spectrum is composed of two signals, which correspond to geometrically different C−D groups on the anthracene (Figure 6e,f), the line shape (Figure 6) of which does not change from 203 K up to 525 K. However, the C−D groups on the bulky anthracene ring are also different in terms of their capability to sense dynamics. The angle between the C−D bond and the rotational axis (the C_2 symmetry axis along C9 and C10 of the anthracene ring) is 60 degrees for D at positions 2, 3, 6, and 7, i.e., the same as for a typical phenylene group, and is 0 degree for the C−D groups at positions 1, 4, 5, and 8. The latter will not sense any motion around the rotational axis due to its angular configuration.[48] Therefore, the line shape splits into a pattern with $Q_1 = 153$ kHz and an asymmetry parameter $\eta_1 = 0.08$ for the C−D groups at 2, 3, 6, and 7 positions, and a pattern with typical static parameters $Q_2 = 176$ kHz and $\eta_2 = 0.0$ for the C−D groups at the 1, 4, 5, and 8 positions. Since the line shapes do not change within this temperature range, no large-amplitude
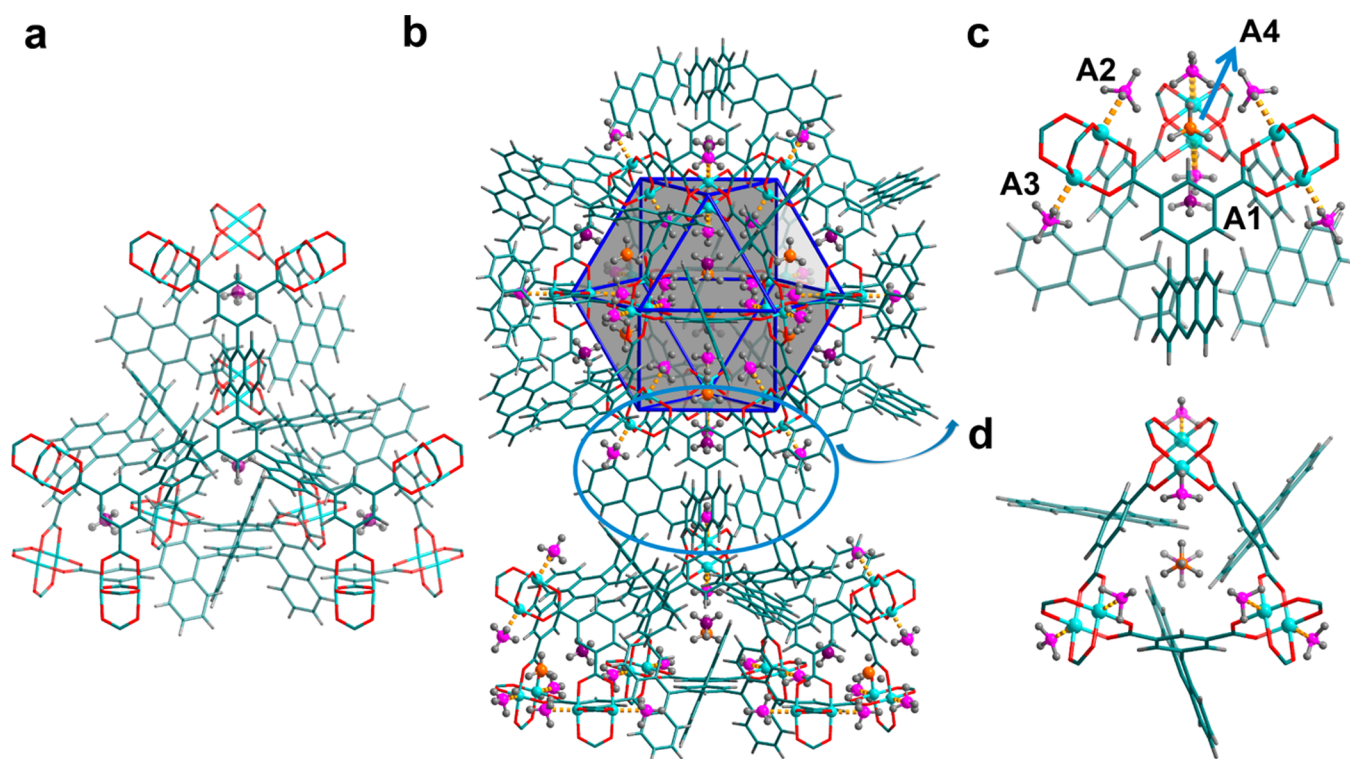
Figure 7. CD_4 adsorption sites revealed by Rietveld analysis of the NPD data for MFM-132a with CD_4 dosing at 0.25 and 0.5 CD_4/Cu. (a) The strongest CD_4 binding site is located in the small pocket created by the $[(Cu_2)_3(isophthalate)_3]$ window and three anthracene rings. There are four of this type of pocket in a truncated tetrahedron (cage **B**). (b) The four binding sites within the partial structure showing cage **A** and cage **B**, both sharing the triangular $[(Cu_2)_3(isophthalate)_3]$ window. (c) Side and (d) top-down view of the tight pocket created by the $[(Cu_2)_3(isophthalate)_3]$ window and three anthracene rings. The two Cu(II) ions on the same $[Cu_2(O_2CR)_4]$ paddlewheel show similar CD_4 binding. Color scheme: C, teal; H, gray; Cu, aqua; site **A1**, violet; sites **A2** and **A3**, pink; site **A4**, orange.

motions are present. But the slightly averaged pattern of the terminal C–D group indicates that the anthracene fragments are in fact involved in fast but limited ($\Delta\varphi = 32°$) angular librations. Similar librations of organic groups in porous materials have been observed recently for ZIF-8.[49] The CH_4-loaded sample of MFM-132a-d_{24} (10 bar of equilibrium pressure above the MOF at 298 K in a sealed glass NMR cell), as for MFM-115a-d_{12}, shows identical line shape and temperature dependence to the guest-free material.

NMR Spectroscopic Summary. Comparison of the NMR spectroscopic results shows that the least sterically hindered phenylene rings in MFM-112a-d_{12} are involved in full 360° rotation around the C_2 symmetry axis and are static only for $T < 100$ K; the intermediate region occurs around 153 K, and these rings show fast motion at $T > 203$ K. In the case of MFM-115a-d_{12}, the full axial rotation of the deuterated phenylene rings persists, but the whole dynamic range is shifted to higher temperature by ~150 K. Thus, there is no rotation at 200 K, with the intermediate stage occurring around 300 K, with the fast limit reached above 403 K. The greater steric confinement of the branched phenylene rings in the hexacarboxylate linkers in MFM-115a-d_{12} compared to MFM-112a-d_{12} is well described by the activation barriers of the rotation: 40 kJ mol^{-1} for MFM-115a-d_{12} versus 8.6 kJ mol^{-1} for MFM-112a-d_{12}. This is also consistent with the geometric environment of the branched phenylene rings in MFM-112 and MFM-115 obtained from the single-crystal X-ray structural analysis. Two distances are thus defined: d_1 is the distance between the closest hydrogens of the mobile fragment and the nonrotating central core in the ligand face, while d_2 is the distance between the closest hydrogens of

two neighboring mobile fragments (Figure 4). When the central phenyl core in the hexacarboxylate unit in MFM-112 is replaced with a nitrogen atom in MFM-115, the shortest possible distance between the phenylene hydrogens decreases from 1.9 Å (d_1 in MFM-112) to 0.8 Å (d_2 in MFM-115), thereby creating a considerably tighter confinement for the phenylene ring rotation in MFM-115.

In contrast, the NMR spectroscopic analysis of MFM-132a-d_{24} confirms that no full rotation of the anthracene rings is possible due to the steric hindrance of neighboring anthracene rings in this (3,24)-connected network. Indeed, no notable motion was detected up to the thermal decomposition of the material at $T > 567$ K. However, the observed line shapes show that the anthracene rings are not completely static, being involved in fast but limited angular librations. Thus, for MFM-132a, the steric restriction is sufficient to render the anthracene group almost immobilized in a well-defined position.

In situ ^{2}H NMR spectra for the three samples loaded with CH_4 were collected to probe the effect of CH_4 adsorption on the rotational molecular dynamics of the frameworks. The line shape analysis indicates that the ligand rotation in MFM-112a-d_{12} is affected by the adsorption of CH_4, revealing a reduced rate of rotation. This indicates that CH_4 interacts with linkers by random collision and inhibits the rotation in the range $T = 123-203$ K. In contrast, addition of CH_4 to MFM-115a-d_{12} (or to MFM-132a-d_{24}, where there is only libration) causes no observed changes to the rotation of the phenylene groups. Rotation for MFM-115a-d_{12} occurs over the range $T = 203-403$ K, much higher than for MFM-112a-d_{12}, and it appears that rotation of phenylene groups at this elevated temperature will
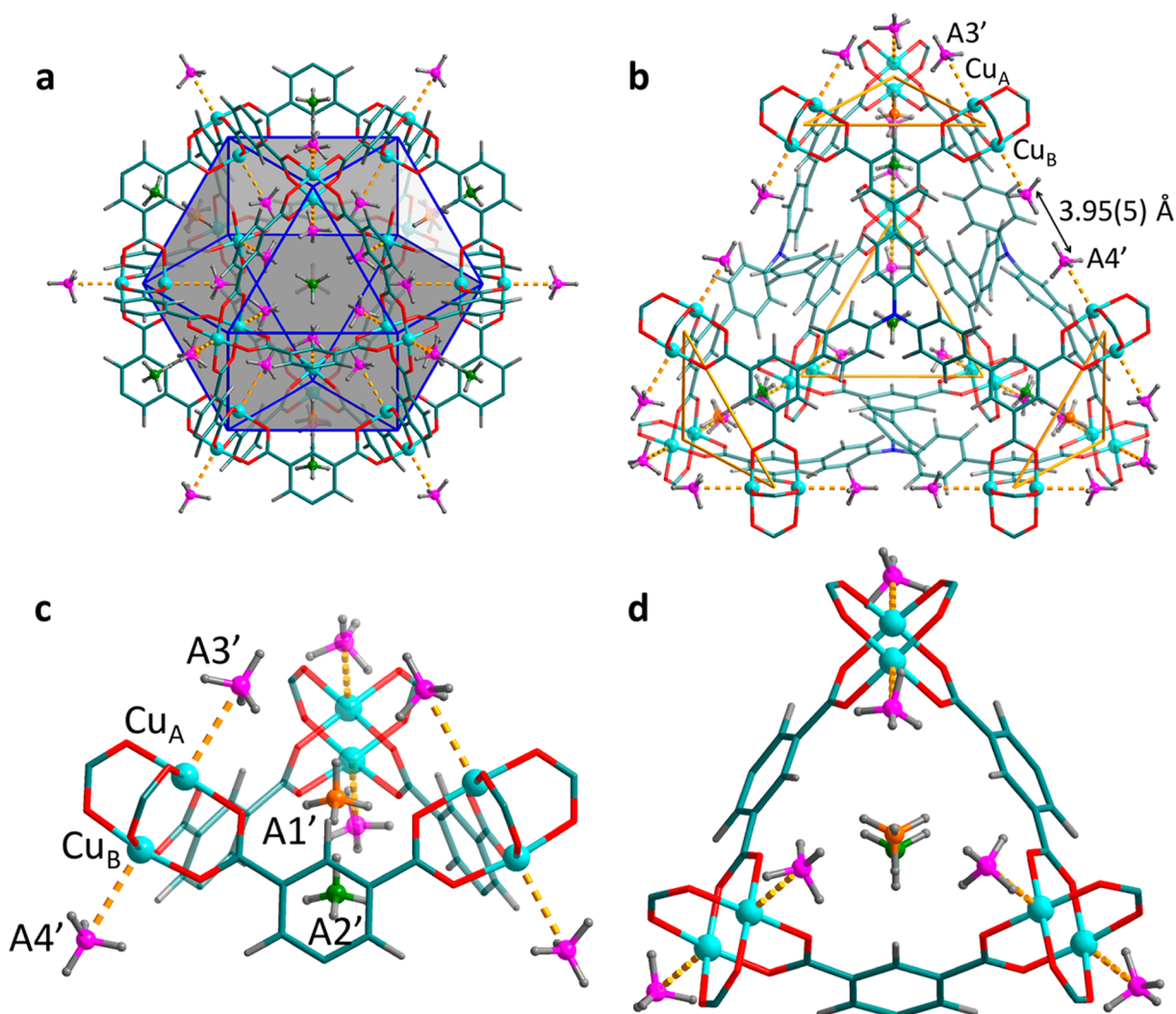
Figure 8. CD_4 adsorption sites in MFM-115a revealed by neutron powder diffraction at a loading of 1.0 CD_4/Cu. (a) CD_4 sites in the cuboctahedral cage showing CD_4 molecules are compacted within this cage. (b) CD_4 sites within the partial structure of a tetrahedral cage. Due to the shorter distance between the two opposite $[Cu_2(O_2CR)_4]$ paddlewheels in cage **D** (on the edge of the tetrahedron) in MFM-115a compared with that in MFM-132a, the two CD_4 sites (**A4′**) show a close contact of 3.95(5) Å. (c) Close view of the four binding sites. Site **A1′** sits within the tight pocket created by three CD_4 on site **A3′** and one CD_4 on site **A2′**, indicating an optimum packing geometry of CD_4 molecules in MFM-115a. (d) Top-down view of the small triangular window. Color scheme: C, teal; H, gray; Cu, aqua; site **A1′**, orange; site **A2′**, green; sites **A3′** and **A4′**, pink.

therefore not be effected by the relatively low energy collisions with CH_4 molecules.

Neutron Powder Diffraction (NPD) Studies. The locations of adsorbed molecules within MFM-132a and MFM-115a were determined by *in situ* NPD as a function of CD_4 loading. NPD patterns were recorded at 10 K for the desolvated materials and at loadings of 0.25 and 0.5 CD_4/Cu for MFM-132a and of 1.0 and 1.5 CD_4/Cu for MFM-115a (see Supporting Information Section 6). MFM-132a shows highly hindered cage geometry and restricted molecular dynamics owing to the anthracene functionalization and was therefore selected for the investigation of CH_4 binding at low loading where adsorption is dominated by pore geometry and surface chemistry. In parallel, CH_4 binding at higher surface coverage was studied in MFM-115a, which displays a record high CH_4 storage capacity, in order to probe the distribution of CH_4 within the structure to a wider extent. Fourier difference map analysis of the NPD data of the desolvated MOFs indicates no residual nuclear density peak in the pore, thus confirming the effective activation and structural stability of the desolvated

samples. Upon loading of the targeted amount of CD_4 into the desolvated MOFs, sequential Fourier difference map analysis revealed the position of the center of mass of the adsorbed CD_4 molecules, which were further developed by Rietveld refinement of these data. Analysis of the lattice parameters of gas-loaded MOFs confirms the absence of notable structural changes.

For MFM-132a at 0.25 CD_4/Cu loading, Rietveld analysis revealed four distinct CD_4 binding sites, the strongest of which was located in the $[(Cu_2)_3(isophthalate)_3]$ window pocket (denoted site **A1**; Figure 7). The cavity formed by three isophthalate rings and the enclosed anthracene moieties shows an internal void with a diameter of only ~6 Å, which can accommodate only one CD_4 molecule; this molecule sits on the C_3-axis of the pocket at a distance of 3.88(1) Å from the center of the isophthalate ring. The three anthracene units at the bottom of the pocket further stabilize the CD_4 molecule via strong space confinement with a close distance of 2.41(1) Å between the D atoms of CD_4 and the H atoms on the anthracene rings. Significantly, nearly 50% of loaded CD_4 is

found on site **A1**, confirming the presence of strongly geometrical-hindered binding sites in MFM-132a. In addition, ~40% of loaded CD_4 is found equally distributed on the two open Cu(II) sites with one protruding into the cuboctahedral cage while the other is pointing outside the cage, denoted as the second (**A2**) and third (**A3**) binding sites, respectively. Thus, in the case of MFM-132a, a tight pocket constructed solely from aromatic rings that matches the symmetry of a CD_4 molecule shows higher affinity for CD_4 than open Cu(II) sites. Importantly, the open Cu(II) centers in MOFs are found not to be the strongest binding site for adsorbed methane molecules, and this may be in part due to the introduction of steric hindrance within the pores of the MOF.

The fourth adsorption site (**A4**) is located inside the cuboctahedron and near the $[(Cu_2)_3(isophthalate)_3]$ window with a distance of 3.56(6) Å from the **A1** site and accounts for ~10% of loaded CD_4. The CD_4 molecule on this site also sits on the 3-fold axis of the triangular window. **A4** also shows close contacts $[CD_4 \text{ (centroid)} \cdots CD_4 \text{ (centroid)} = 3.84(6) \text{ Å}]$ with the CD_4 molecules on site **A2**. The CD_4 on site **A4** therefore occupies the pocket created by the three CD_4 molecules adsorbed on the three closest open Cu(II) sites of the triangular window and the encapsulated CD_4 within the small 6 Å cavity (site **A1**), indicating the presence of intermolecular adsorbate–adsorbate interaction that stabilizes the packing of methane molecules in the structure. No additional site was identified at the higher loading of 0.5 CD_4/Cu, where the occupancies for all four binding sites increase proportionately. Notably, the **A1** site occupancy remains the highest of the four sites identified, further confirming the strong affinity between CD_4 molecules and this tight pocket.

The NPD study of MFM-115a at both 1.0 and 1.5 CD_4/Cu loadings revealed four binding sites (denoted **A1′**, **A2′**, **A3′**, and **A4′** in order of decreasing occupancy; Figure 8). **A1′** and **A2′** are found within the triangular $[(Cu_2)_3(isophthalate)_3]$ window, and **A3′** and **A4′** are located on the open Cu(II) sites. At the first loading, site **A1′** is located on the 3-fold axis of the $[(Cu_2)_3(isophthalate)_3]$ window. This is not surprising because site **A1′** sits in the tight pocket created by three CD_4 molecules on site **A3′** and one CD_4 on site **A2′**, indicating the presence of strong intermolecular dipole interaction. Site **A2′** also resides on the 3-fold axis of the small triangular window, having a similar location to the strongest adsorption site **A1** observed in MFM-132a, but with a longer distance of 4.34(3) Å to the center of the isophthalate ring. The reduction in binding affinity of **A2′** in MFM-115a is a direct result of the absence of a tight cavity formed by organic moieties as found in MFM-132a. To our surprise, the two types of open Cu(II) sites in MFM-115a have distinct occupancies, with the one located inside the cuboctahedral cage showing almost five times the occupancy as the other one outside this cage. This observation indicates that 12 methane molecules inside the cuboctahedral cage show a compact geometry in MFM-115a. The two opposite $[Cu_2(O_2CR)_4]$ paddlewheels in cage **D** are separated by a shorter distance in MFM-115a than in MFM-132a due to the smaller size of the hexacarboxylate ligand in the former. This effectively accounts for the difference of CD_4 binding behavior on the open Cu(II) sites in these two structures. Thus, the distance between two opposite Cu(II) sites in cage **D** in MFM-115a is 3.95(5) Å, much shorter than that $[6.83(5) \text{ Å}]$ observed in MFM-132a. At the 1.5 CD_4/Cu loading, additional CD_4 molecules are mainly populated across sites **A1′**, **A2′**, and **A3′**,

further indicating a unique and optimized CD_4 packing geometry in MFM-115a.

■ CONCLUSIONS

A family of isostructural (3,24)-connected frameworks, MFM-112a, MFM-115a, and MFM-132a, shows interesting and distinct CH_4 adsorption properties. The overall structures of these materials are constructed by alternate packing of four types of metal–organic coordination cages with varying geometry and sizes. Specifically, MFM-132 contains a type of highly geometrically hindered cages (diameter of ~6 Å) because of the anthracene functionalization. MFM-112a, MFM-115a, and MFM-132a possess high, moderate, and relatively low porosity, respectively. Significantly, MFM-115a displays exceptionally high deliverable CH_4 storage capacity $[208 \text{ v/v } (5-80 \text{ bar})]$ at room temperature, comparable with the best performing porous solids reported to date. MFM-112a also reveals excellent CH_4 adsorption capacity at high pressure owing to its high surface area and pore volume. In contrast, MFM-132a shows relatively low CH_4 storage capacity. Thus, there is a direct correlation between the structure design and materials function across this series of MOFs.

The molecular motions of the rotating aromatic rings in the corresponding partially deuterated materials MFM-112a-d_{12}, MFM-115a-d_{12}, and MFM-132a-d_{24} were investigated using *in situ* solid-state ^{2}H NMR spectroscopy. The results reveal that the branched phenylene ring rotation in MFM-115a-d_{12} shows an energy barrier that is almost 5 times higher than that in MFM-112a-d_{12}. The anthracene ring in MFM-132a-d_{24} shows very limited angular librations within its confinement, which allows the anthracene rings to form stable well-defined cavities within the framework. The CH_4 loading affects the ligand rotation in MFM-112a-d_{12} slightly, but does not pose any notable hindrance for the ligand mobility in MFM-115a-d_{12} and MFM-132a-d_{24}. The NMR spectroscopic study confirms that MFM-112a, MFM-115a, and MFM-132a have fast, medium, and slow molecular dynamics, respectively. Investigations on the binding sites for CD_4 within MFM-132a and MFM-115a reveal that the primary binding site is located within the small pocket enclosed by the $[(Cu_2)_3(isophthalate)_3]$ window and three anthracene/phenyl panels. This pocket shows strong van der Waals interactions with CD_4 due to the small cavity size and has an excellent size and geometric match for a single CD_4 molecule. The open Cu(II) sites are the secondary/tertiary adsorption sites in these structures. Thus, direct experimental evidence has been obtained showing that a tight cavity can generate a stronger binding affinity for gas molecules than open metal sites, which are widely reported as the primary binding sites in various MOFs. Thus, the NPD coupled with ^{2}H NMR spectroscopy confirms that a combination of optimum molecular dynamics and pore geometry/size leads to the interesting CH_4 adsorption performance in these materials.

■ EXPERIMENTAL SECTION

Synthesis of MFM-112 and MFM-115. MFM-112 and MFM-115 were synthesized following the methods adapted from previous reports.[22,24b] Specifically, a solution of H_6TDBB (1,3,5-tris(3′,5′-dicarboxy[1,1′-biphenyl]-4-yl)benzene) (or H_6NTBD = 4′,4″,4‴-nitrilotribiphenyl-3,5-dicarboxylic acid, 0.1 mmol, 1.0 equiv) and $Cu(NO_3)_2 \cdot 2.5H_2O$ (93 mg, 4.0 equiv) in N,N-dimethylformamide (DMF, 40 mL) and H_2O (4 mL) was placed in a 100 mL pressure flask. To the mixture was added 2M HCl (0.5mL), and the pressure flask was sealed and heated at 90 °C in an oil bath for 24 h. The

obtained crystals were filtered and washed with DMF (20 mL × 2). The as-synthesized materials were exchanged in acetone for 3 days before being activated for gas sorption experiments.

Synthesis of [Cu$_3$(BTAT)(H$_2$O)$_3$]·9DMF (MFM-132). H$_6$BTAT (50 mg, 0.045 mmol) (see Supporting Information Section S1) and Cu(NO$_3$)$_2$·2.5H$_2$O (63 mg, 0.27 mmol) were dissolved in a mixture of DMF (8.0 mL) and H$_2$O (0.5 mL), and the solution placed in a pressure tube (15 mL). Upon addition of 6 M HCl (15 μL), the tube was capped and heated at 90 °C for 16 h. A large amount of microcrystalline product precipitated: the blue crystals were collected by filtration and washed with warm DMF and dried in air. Yield: 77 mg (85%). Selected FTIR (neat, cm^{-1}): 1655 (vs), 1632 (vs), 1587 (w), 1493 (w), 1434 (s), 1366 (s), 1299 (w), 1253 (m), 1195 (w), 1149 (w), 1095 (s), 1060 (w), 1027 (w), 942 (w), 922 (w), 864 (w), 774 (vs), 734 (m), 701 (m), 660 (s), 648 (m). Anal. Calcd (%) for C$_{99}$H$_{105}$Cu$_3$N$_9$O$_{24}$: C, 59.59; H, 5.30; N, 6.32. Found (%): C, 60.38; H, 5.31; N, 6.78.

High-Pressure CH$_4$ Adsorption Measurements. CH$_4$ sorption measurements (0−90 bar) were performed using a XEMIS gravimetric adsorption apparatus (Hiden Isochema, Warrington, UK) equipped with a clean ultra-high-vacuum system. The pressure in the system is accurately regulated by mass flow controllers. All measurements were made with ultra-high-purity grade (99.999%) CH$_4$ or He, the latter being used for framework skeletal volume measurements. Sample containers of a known weight were loaded with ∼100 mg of desolvated sample under Ar, and the samples were further degassed at 100 °C for 16 h before adsorption of CH$_4$.

Solid-State ^{2}H NMR Spectroscopy. To prepare samples for the NMR experiments, 50−70 mg of partially deuterated MOF was loaded as a fine powder into a 5 mm (o.d.) glass tube and connected to a high-vacuum line. The sample was heated at 100 °C for 24 h under vacuum to a final pressure above the sample of 10^{-2} Pa to ensure removal of any remaining traces of guest molecules. The neck of the tube was then flame-sealed, while the sample was maintained in liquid nitrogen in order to prevent the heating from the flame. The sealed sample was then transferred into an NMR probe for analysis with ^{2}H NMR spectroscopy.

^{2}H NMR spectroscopic experiments were performed at the Larmor frequency $\omega_z/2\pi$ = 61.42 MHz on a Bruker Avance-400 spectrometer using a high-power probe with 5 mm horizontal solenoid coil. All ^{2}H NMR spectra were obtained by Fourier transformation of the quadrature-detected phase-cycled quadrupole echo arising in the pulse sequence $(90^\circ_x - \tau_1 - 90^\circ_y - \tau_2 - \text{acquisition} - t)$, where τ_1 = 20 μs, τ_2 = 21 μs, and t is the repetition time of the sequence during the accumulation of the NMR signal.[50] The duration of the $\pi/2$ pulse was 1.6 μs. Spectra were typically obtained with 1000−20000 scans with a repetition time of ∼0.4 s. The temperature of the samples was controlled with a flow of N$_2$ gas using a BVT-3000 variable-temperature unit with a precision of ∼1 K. The ^{2}H NMR spectra line shape simulations were performed using an in-house FORTRAN program package based on the general formalism given in the Supporting Information Section S5.

Neutron Powder Diffraction. NPD measurements were performed on the bare MOF and the same sample loaded with CD$_4$ using the WISH high-resolution powder diffractometer at the ISIS pulsed neutron source, Rutherford Appleton Laboratory, UK. Prior to NPD experiments, the desolvated sample of MFM-132a (1.4 g) or MFM-115a (1.8 g) was loaded into a cylindrical vanadium sample container with an indium ring vacuum seal and connected to a gas handling system. The sample was further degassed at 10^{-7} mbar and 100 °C for 24 h to remove any remaining trace guest solvents. The temperature during data collection was controlled using a helium cryostat operating at 10 ± 0.2 K. The loadings of CD$_4$ were performed by a volumetric method at 150 K in order to ensure that CD$_4$ was present in the gas phase when not adsorbed and also to ensure sufficient mobility of CD$_4$ inside the crystalline structure. After collecting the NPD data for the bare material, target amounts of CD$_4$ were introduced from the gas-panel system. The sample was then slowly cooled (over a period of 2 h) to 10 K to ensure that CD$_4$ was completely adsorbed. Sufficient time was allowed to achieve thermal

equilibrium before data collection. Time-of-flight neutron diffraction data were collected by five detector banks centered at 2θ = 27.1°, 58.3°, 90.0°, 121.7°, and 152.9°.

Due to the large unit cell of these two frameworks, rigid bodies were applied to the organic ligand and the CD$_4$ molecules in the Rietveld refinements. Difference Fourier maps calculated from neutron diffraction data were used to locate the adsorbed CD$_4$ molecules. The refinements on all the parameters including fractional coordinates, occupancies for the adsorbed CD$_4$ molecules, and background/profile coefficients yielded satisfactory agreement factors. The total occupancies of CD$_4$ molecules obtained from the refinement are also in good agreement with the experimental values for the CD$_4$ loading. The refined structural parameters including the refined positions of the CD$_4$ molecules are detailed in the Supporting Information Section S6.

■ ASSOCIATED CONTENT

⑤ Supporting Information

The Supporting Information is available free of charge on the ACS Publications website at DOI: 10.1021/jacs.7b05453.

> Synthetic details for organic linkers and partially deuterated compounds; gas adsorption data; solid-state ^{2}H NMR spectroscopic and neutron powder diffraction analysis (PDF)

■ AUTHOR INFORMATION

Corresponding Authors
*Sihai.Yang@manchester.ac.uk
*M.Schroder@manchester.ac.uk

ORCID ⊙
Alexander G. Stepanov: 0000-0003-2754-5273
Martin Schröder: 0000-0001-6992-0700

Author Contributions
¶Y. Yan, D. I. Kolokolov, and I. da Silva contributed equally to this work.

Notes
The authors declare no competing financial interest.
CIF files can be obtained free of charge from the Cambridge Crystallographic Data Centre via www.ccdc.cam.ac.uk/data_request/cif (CCDC 1499823−1499831).

■ ACKNOWLEDGMENTS

■ REFERENCES

(1) Service, R. F. *Science* **2014**, *346*, 538−541.
(2) Yeh, S. *Energy Policy* **2007**, *35*, 5865−5875.
(3) International Energy Agency, World Energy Outlook 2011: Are We Entering a Golden Age of Gas, http://www.worldenergyoutlook.org.

(4) Makal, T. A.; Li, J.-R.; Lu, W.; Zhou, H.-C. *Chem. Soc. Rev.* **2012**, *41*, 7761−7779.

(5) Lin, X.; Jia, J.; Hubberstey, P.; Schröder, M.; Champness, N. R. *CrystEngComm* **2007**, *9*, 438−448.

(6) Murray, L. J.; Dincă, M.; Long, J. R. *Chem. Soc. Rev.* **2009**, *38*, 1294−1314.

(7) Mason, J. A.; Veenstra, M.; Long, J. R. *Chem. Sci.* **2014**, *5*, 32−51.

(8) He, Y.; Zhou, W.; Qian, G.; Chen, B. *Chem. Soc. Rev.* **2014**, *43*, 5657−5678.

(9) Li, J.-R.; Sculley, J.; Zhou, H.-C. *Chem. Rev.* **2012**, *112*, 869−932.

(10) Bloch, E. D.; Queen, W. L.; Krishna, R.; Zadrozny, J. M.; Brown, C. M.; Long, J. R. *Science* **2012**, *335*, 1606−1610.

(11) Yang, S.; Sun, J.; Ramirez-Cuesta, A. J.; Callear, S. K.; David, W. I. F.; Anderson, D. P.; Newby, R.; Blake, A. J.; Parker, J. E.; Tang, C. C.; Schröder, M. *Nat. Chem.* **2012**, *4*, 887−894.

(12) Kreno, L. E.; Leong, K.; Farha, O. K.; Allendorf, M.; Van Duyne, R. P.; Hupp, J. T. *Chem. Rev.* **2012**, *112*, 1105−1125.

(13) Zhao, M.; Ou, S.; Wu, C.-D. *Acc. Chem. Res.* **2014**, *47*, 1199−1207.

(14) Cui, Y.; Li, B.; He, H.; Zhou, W.; Chen, B.; Qian, G. *Acc. Chem. Res.* **2016**, *49*, 483−493.

(15) Furukawa, H.; Cordova, K. E.; O'Keeffe, M.; Yaghi, O. M. *Science* **2013**, *341*, 974−986.

(16) Zhao, D.; Timmons, D. J.; Yuan, D.; Zhou, H.-C. *Acc. Chem. Res.* **2011**, *44*, 123−133.

(17) Guillerm, V.; Kim, D.; Eubank, J. F.; Luebke, R.; Liu, X.; Adil, K.; Lah, M. S.; Eddaoudi, M. *Chem. Soc. Rev.* **2014**, *43*, 6141−6172.

(18) (a) Easun, T. L.; Moreau, F.; Yan, Y.; Yang, S.; Schröder, M. *Chem. Soc. Rev.* **2017**, *46*, 239−274. (b) Zhang, J.-P.; Liao, P.-Q.; Zhou, H.-L.; Lin, R.-B.; Chen, X.-M. *Chem. Soc. Rev.* **2014**, *43*, 5789−5814.

(19) Methane Opportunities for Vehicular Energy, Advanced Research Project Agency − Energy, U.S. Dept. of Energy, Funding Opportunity No. DE-FOA-0000672, 2012. https://arpa-e-foa.energy.gov/Default.aspx?Search=DE-FOA-0000672.

(20) Yan, Y.; Yang, S.; Blake, A. J.; Schröder, M. *Acc. Chem. Res.* **2014**, *47*, 296−307.

(21) Farha, O. K.; Yazaydın, A. Ö.; Eryazici, I.; Malliakas, C. D.; Hauser, B. G.; Kanatzidis, M. G.; Nguyen, S. T.; Snurr, R. Q.; Hupp, J. T. *Nat. Chem.* **2010**, *2*, 944−948.

(22) Yan, Y.; Lin, X.; Yang, S.; Blake, A. J.; Dailly, A.; Champness, N. R.; Hubberstey, P.; Schröder, M. *Chem. Commun.* **2009**, *9*, 1025−1027.

(23) Yan, Y.; Telepeni, I.; Yang, S.; Lin, X.; Kockelmann, W.; Dailly, A.; Blake, A. J.; Lewis, W.; Walker, G. S.; Allan, D. R.; Barnett, S. A.; Champness, N. R.; Schröder, M. *J. Am. Chem. Soc.* **2010**, *132*, 4092−4094.

(24) (a) Yan, Y.; Suyetin, M.; Bichoutskaia, E.; Blake, A. J.; Allan, D. R.; Barnett, S. A.; Schröder, M. *Chem. Sci.* **2013**, *4*, 1731−1736. (b) Yan, Y.; Blake, A. J.; Lewis, W.; Barnett, S. A.; Dailly, A.; Champness, N. R.; Schröder, M. *Chem. - Eur. J.* **2011**, *17*, 11162−11170.

(25) Yuan, D.; Zhao, D.; Sun, D.; Zhou, H.-C. *Angew. Chem., Int. Ed.* **2010**, *49*, 5357−5361.

(26) Wu, H.; Simmons, J. M.; Liu, Y.; Brown, C. M.; Wang, X.-S.; Ma, S.; Peterson, V. K.; Southon, P. D.; Kepert, C. J.; Zhou, H.-C.; Yildirim, T.; Zhou, W. *Chem. - Eur. J.* **2010**, *16*, 5205−5214.

(27) Hulvey, Z.; Vlaisavljevich, B.; Mason, J. A.; Tsivion, E.; Dougherty, T. P.; Bloch, E. D.; Head-Gordon, M.; Smit, B.; Long, J. R.; Brown, C. M. *J. Am. Chem. Soc.* **2015**, *137*, 10816−10825.

(28) Getzschmann, J.; Senkovska, I.; Wallacher, D.; Tovar, M.; Fairen-Jimenez, D.; Düren, T.; van Baten, J. M.; Krishna, R.; Kaskel, S. *Microporous Mesoporous Mater.* **2010**, *136*, 50−58.

(29) Wu, H.; Zhou, W.; Yildirim, T. *J. Am. Chem. Soc.* **2009**, *131*, 4995−5000.

(30) Spek, A. L. *Acta Crystallogr., Sect. D: Biol. Crystallogr.* **2009**, *65*, 148−155.

(31) Peng, Y.; Krungleviciute, V.; Eryazici, I.; Hupp, J. T.; Farha, O. K.; Yildirim, T. *J. Am. Chem. Soc.* **2013**, *135*, 11887−11894.

(32) He, Y.; Zhou, W.; Yildirim, T.; Chen, B. *Energy Environ. Sci.* **2013**, *6*, 2735−2744.

(33) Wang, X.-S.; Ma, S.; Rauch, K.; Simmons, J. M.; Yuan, D.; Wang, X.; Yildirim, T.; Cole, W. C.; López, J. J.; de Meijere, A.; Zhou, H.-C. *Chem. Mater.* **2008**, *20*, 3145−3152.

(34) Kennedy, R. D.; Krungleviciute, V.; Clingerman, D. J.; Mondloch, J. E.; Peng, Y.; Wilmer, C. E.; Sarjeant, A. A.; Snurr, R. Q.; Hupp, J. T.; Yildirim, T.; Farha, O. K.; Mirkin, C. A. *Chem. Mater.* **2013**, *25*, 3539−3543.

(35) Gándara, F.; Furukawa, H.; Lee, S.; Yaghi, O. M. *J. Am. Chem. Soc.* **2014**, *136*, 5271−5274.

(36) Ma, S.; Sun, D.; Simmons, J. M.; Collier, C. D.; Yuan, D.; Zhou, H.-C. *J. Am. Chem. Soc.* **2008**, *130*, 1012−1016.

(37) Wilmer, C. E.; Farha, O. K.; Yildirim, T.; Eryazici, I.; Krungleviciute, V.; Sarjeant, A. A.; Snurr, R. Q.; Hupp, J. T. *Energy Environ. Sci.* **2013**, *6*, 1158−1163.

(38) Mason, J. A.; Oktawiec, J.; Taylor, M. K.; Hudson, M. R.; Rodriguez, J.; Bachman, J. E.; Gonzalez, M. I.; Cervellino, A.; Guagliardi, A.; Brown, C. B.; Llewellyn, P. L.; Masciocchi, N.; Long, J. R. *Nature* **2015**, *527*, 357−361.

(39) Li, B.; Wen, H.-M.; Wang, H.; Wu, H.; Tyagi, M.; Yildirim, T.; Zhou, W.; Chen, B. *J. Am. Chem. Soc.* **2014**, *136*, 6207−6210.

(40) Jiang, J.; Furukawa, H.; Zhang, Y.-B.; Yaghi, O. M. *J. Am. Chem. Soc.* **2016**, *138*, 10244−10251.

(41) Alezi, D.; Belmabkhout, Y.; Suyetin, M.; Bhatt, P. M.; Weseliński, Ł. J.; Solovyeva, V.; Adil, K.; Spanopoulos, I.; Trikalitis, P. N.; Emwas, A.-H.; Eddaoudi, M. *J. Am. Chem. Soc.* **2015**, *137*, 13308−13318.

(42) Spanopoulos, I.; Tsangarakis, C.; Klontzas, E.; Tylianakis, E.; Froudakis, G.; Adil, K.; Belmabkhout, Y.; Eddaoudi, M.; Trikalitis, P. N. *J. Am. Chem. Soc.* **2016**, *138*, 1568−1574.

(43) Furukawa, H.; Ko, N.; Go, Y. B.; Aratani, N.; Choi, S. B.; Choi, E.; Yazaydin, A. Ö.; Snurr, R. Q.; O'Keeffe, M.; Kim, J.; Yaghi, O. M. *Science* **2010**, *329*, 424−428.

(44) Tycko, R. *Nuclear Magnetic Resonance Probes of Molecular Dynamics*; Kluwer Academic Publishers: Dordrecht, The Netherlands, 1994.

(45) (a) Horike, S.; Matsuda, R.; Tanaka, D.; Matsubara, S.; Mizuno, M.; Endo, K.; Kitagawa, S. *Angew. Chem., Int. Ed.* **2006**, *45*, 7226−7230. (b) Gould, S. L.; Tranchemontagne, D.; Yaghi, O. M.; Garcia-Garibay, M. A. *J. Am. Chem. Soc.* **2008**, *130*, 3246−3247. (c) Comotti, A.; Bracco, S.; Sozzani, P. *Acc. Chem. Res.* **2016**, *49*, 1701−1710. (d) Jiang, X.; O'Brien, Z. J.; Yang, S.; Lai, L. H.; Buenaflor, J.; Tan, C.; Khan, S.; Houk, K. N.; Garcia-Garibay, M. A. *J. Am. Chem. Soc.* **2016**, *138*, 4650−4656. (e) Comotti, A.; Bracco, S.; Yamamoto, A.; Beretta, M.; Hirukawa, T.; Tohnai, N.; Miyata, M.; Sozzani, P. *J. Am. Chem. Soc.* **2014**, *136*, 618−621. (f) Comotti, A.; Bracco, S.; Ben, T.; Qiu, S.; Sozzani, P. *Angew. Chem., Int. Ed.* **2014**, *53*, 1043−1047.

(46) Shustova, N. B.; Ong, T.-C.; Cozzolino, A. F.; Michaelis, V. K.; Griffin, R. G.; Dincă, M. *J. Am. Chem. Soc.* **2012**, *134*, 15061−15070.

(47) Bracco, S.; Miyano, T.; Negroni, M.; Bassanetti, I.; Marchio', L.; Sozzani, P.; Tohnai, N.; Comotti, A. *Chem. Commun.* **2017**, *53*, 7776−7779.

(48) Jelinski, L. W. Deuterium NMR of Solid Polymers. In *High Resolution NMR Spectroscopy of Synthetic Polymers in Bulk*; Komoroski, R. A., Ed.; VCH Publishers: New York, 1986; Vol. 7, p 335.

(49) Kolokolov, D. I.; Stepanov, A. G.; Jobic, H. *J. Phys. Chem. C* **2015**, *119*, 27512−27520.

(50) Powles, J. G.; Strange, J. H. *Proc. Phys. Soc., London* **1963**, *82*, 6−15.